

Identifying the effect of photo-generated carriers on the phonons in rutile TiO_2 through Raman spectroscopy

Zheng Wang(王征), Min Liao(廖敏), Guihua Wang(王桂花), and Meng Zhang(张梦)

Citation: Chin. Phys. B, 2024, 33 (**11**): 117802. DOI: 10.1088/1674-1056/ad73b4
Journal homepage: http://cpb.iphy.ac.cn; http://iopscience.iop.org/cpb

What follows is a list of articles you may be interested in

Unveiling localized electronic properties of ReS_2 thin layers at nanoscale using Kelvin force probe microscopy combined with tip-enhanced Raman spectroscopy

Yu Luo(罗宇), Weitao Su(苏伟涛), Juanjuan Zhang(张娟娟), Fei Chen(陈飞), Ke Wu(武可), Yijie Zeng(曾宜杰), and Hongwei Lu(卢红伟)
Chin. Phys. B, 2023, 32 (**11**): 117801. DOI: 10.1088/1674-1056/ace425

Raman spectroscopy of isolated carbyne chains confined in carbon nanotubes: Progress and prospects

Johannes M. A. Lechner, Pablo Hernández López, and Sebastian Heeg
Chin. Phys. B, 2022, 31 (**12**): 127801. DOI: 10.1088/1674-1056/ac9608

Synthesis of ternary compound in H-S-Se system at high pressures

Xiao Zhang(张晓)
Chin. Phys. B, 2021, 30 (**12**): 127801. DOI: 10.1088/1674-1056/abf7aa

Signal-to-noise ratio of Raman signal measured by multichannel detectors

Xue-Lu Liu(刘雪璐), Yu-Chen Leng(冷宇辰), Miao-Ling Lin(林妙玲), Xin Cong(从鑫), and Ping-Heng Tan(谭平恒)
Chin. Phys. B, 2021, 30 (**9**): 097807. DOI: 10.1088/1674-1056/ac1f06

Achieving high-performance multilayer $MoSe_2$ photodetectors by defect engineering

Jintao Hong(洪锦涛), Fengyuan Zhang(张丰源), Zheng Liu(刘峥), Jie Jiang(蒋杰), Zhangting Wu(吴章婷), Peng Zheng(郑鹏), Hui Zheng(郑辉), Liang Zheng(郑梁), Dexuan Huo(霍德璇), Zhenhua Ni(倪振华), and Yang Zhang(张阳)
Chin. Phys. B, 2021, 30 (**8**): 087801. DOI: 10.1088/1674-1056/abea8b

---

Identifying the effect of photo-generated carriers on the phonons in rutile TiO_2 through Raman spectroscopy

Zheng Wang(王征), Min Liao(廖敏), Guihua Wang(王桂花), and Meng Zhang(张梦)†

School of Electronic and Information Engineering, Beihang University, Beijing 100191, *China*

(Received 27 June 2024; revised manuscript received 6 August 2024; accepted manuscript online 27 August 2024)

Investigating lattice vibrations through Raman spectroscopy is a crucial method for studying crystalline materials. Carriers can interact with lattices and influence lattice vibrations; thus, it is feasible to study the effect of photo-generated carriers on phonons by analyzing changes in the Raman spectra of semiconductors. Rutile is one of the predominant crystalline phases of TiO_2, which is a widely utilized metal oxide semiconductor. In this work, rutile TiO_2 is coated on a thinned optical fiber to concentrate ultraviolet light energy within the material, thereby enhancing the generation of carriers and amplifying the changes in the Raman spectra. A Raman detection laser with a wavelength of 532 nm is utilized to collect the Raman spectra of rutile TiO_2 during irradiation. Using this setup, the impact of photo-generated carriers on the phonons corresponding to Raman vibrational modes is researched. The localization and non-radiative recombination of photo-generated carriers contribute to a reduction in both the frequencies and lifetimes of phonons. This work provides a novel approach to researching the effect of carriers on phonons.

Keywords: Raman spectroscopy, photo-generated carriers, rutile TiO_2, phonons

PACS: 78.56.Cd, 74.25.Kc, 74.25.nd, 61.82.Fk **DOI:** 10.1088/1674-1056/ad73b4

1. Introduction

Raman spectroscopy is an optimal non-destructive technique for investigating microscopic structures.[1–3] Each Raman peak corresponds to a specific lattice vibrational mode (phonon), while the alterations in the lattice structure can be elucidated by analyzing the changes of Raman peaks.[4,5] The generation of carriers in semiconductors through photo-excitation can be applied in various fields, such as pollutant degradation,[6] water decomposition,[7] sterilization,[8] and solar cells.[9] Researching the behavior of photo-generated carriers serves as a fundamental approach for elucidating the working mechanisms of semiconductors. The localization of carriers by lattices induces lattice distortions, which are referred to as polarons.[10,11] The non-radiative recombination of carriers also generates phonons, thereby generating phonon–phonon interaction known as the anharmonic effect.[12,13] Therefore, theoretically, photo-generated carriers can affect the Raman-active vibrational modes in semiconductors, thereby resulting in changes of the Raman spectra. The effect of photo-generated carriers on phonons can be researched through the real-time monitoring of the Raman spectra of semiconductors.

TiO_2 is a wide bandgap (3.0–3.2 eV) metal oxide semiconductor that can be excited by ultraviolet light, offering advantages such as excellent chemical stability, cost-effectiveness, and environmental friendliness.[14,15] Rutile is the most common and stable phase of TiO_2, characterized by a tetragonal crystal structure with space group $P4/mnm$.[16] Rutile TiO_2 has four Raman-active vibrational modes: B_{1g}, E_g, A_{1g}, B_{2g}, with E_g and A_{1g} being the most significant and extensively researched.[17,18] The position and full width at half-maximum (FWHM) of Raman peaks are critical parameters that reflect the frequency and relaxation time of corresponding vibrational modes, respectively.[19] The primary factors influencing the position and FWHM of the Raman peaks for rutile TiO_2 are temperature,[20,21] size,[22] and pressure.[23] Increasing temperature results in red-shifts (shift towards lower wavenumbers) and broadenings of the E_g and A_{1g} peaks. This phenomenon is mainly attributed to the temperature-induced thermal expansion of the lattice, which affects the phonon frequencies and lifetimes. Lan *et al.* subjected rutile TiO_2 to overall heating in a furnace.[24] They observed a significant red-shift of the E_g peak, while the A_{1g} peak exhibited a slight red-shift, the FWHMs of both peaks increased significantly. Zhang *et al.* increased the temperature of the detection spot by elevating the optical power of the Raman detection laser (785 nm), resulting in changes in both the positions and FWHMs of the E_g and A_{1g} peaks in the same manner.[25] Reducing the size of rutile TiO_2 nanocrystals also induces red-shifts and broadenings of the E_g and A_{1g} peaks, which can be attributed to the phonon confinement effect.[26] Pressure results in the positions of the E_g and A_{1g} peaks moving towards higher wavenumbers (blue shift), and concurrently the FWHMs of the two Raman peaks increase. This effect is due to the transformation of the crystal structure of rutile TiO_2 to a disordered baddeleyite structure under pressure.[27] Currently, limited research explores the effect of photo-generated carriers on the Raman spectra of rutile TiO_2.

†Corresponding author. E-mail: mengzhang10@buaa.edu.cn

© 2024 Chinese Physical Society and IOP Publishing Ltd

Enhancing the interaction between ultraviolet light and rutile TiO_2 is essential for promoting the generation of carriers, thereby amplifying the changes in the Raman spectra. Concentrating light energy in rutile TiO_2 is an effective means to achieve this enhancement. Rutile TiO_2 is coated on a thinned optical fiber, where the cross-sectional area is reduced. A portion of the transmitted light can directly interact with rutile TiO_2.[28,29] Moreover, this configuration effectively confines the light field within rutile TiO_2, thereby enhancing the interaction between the excitation light and the material.

In this study, we constructed a Raman testing system aimed at enhancing the impact of photo-generated carriers on Raman spectra by strengthening the interaction between ultraviolet light and rutile TiO_2 utilizing thinned optical fiber. The effects of irradiation duration and intensity on the Raman spectra of rutile TiO_2 were researched. The results demonstrated that irradiation induced red-shifts and broadenings in both the E_g and A_{1g} peaks, indicating a decrease in the frequencies and lifetimes of the corresponding phonons. The red-shifts and broadenings of the two Raman peaks became more pronounced with increasing irradiation intensity, while the impact of irradiation duration was minimal. In conjunction with the density functional theory (DFT) calculations in related references,[30–32] we deduced that the localization and non-radiative recombination of photo-generated carriers were the primary factors driving these changes.

2. Experimental details

Thinned optical fiber was fabricated by flame heating and pulling to reduce the diameter of the silica optical fiber (core/cladding diameters: 3/125 μm). During the flame heating and pulling process, the core and cladding of the optical fiber melted, and the diameter of the thinned region was approximately 20 μm. TiO_2 was coated onto the thinned optical fiber using a hydrothermal method. Initially, the optical fiber was immersed in a seed solution of tetrabutyl titanate dissolved in isopropanol at a concentration of 75 mM for 3 min, followed by annealing at 450 °C for 1 h. The precursor solution for the hydrothermal reaction was prepared by mixing 80 mL of concentrated hydrochloric acid, 80 mL of ultrapure water, and 3.2 mL of tetrabutyl titanate. The hydrothermal reaction was carried out at 180 °C for 5.5 h. Subsequently, the optical fiber coated with TiO_2 was annealed at 500 °C for 1 h to remove organic residues and improve crystallinity. Scanning electron microscopy and transmission electron microscopy (TEM) were used to analyze the morphology and lattice structure of TiO_2. The optical properties of TiO_2 were characterized using UV-visible absorption spectroscopy. The light field distribution of the optical fiber coated with TiO_2 was acquired using optical microscopy.

The Raman spectra of TiO_2 were collected by a confocal Raman spectrometer with a detection laser wavelength of 532 nm. The spectral resolution and repeatability of the Raman spectrometer were less than 0.65 cm^{-1} and ±0.2 cm^{-1}, respectively. The photon energy of the detection laser was 2.33 eV, which is significantly lower than the bandgap of TiO_2, and is thereby incapable of exciting photo-generated carriers. The optical fiber coated with TiO_2 was coupled to a fiber laser source with an output wavelength of 405 nm. A schematic illustration of the Raman testing system is presented in Fig. 1, where the thinned region coated with TiO_2 was positioned under the 532 nm detection laser beam. The focused spot area and optical power of the 532 nm detection laser were 314 μm^2 and 0.025 mW, respectively. The Raman spectrum acquisition range spanned from 350 cm^{-1} to 700 cm^{-1}, covering the E_g and A_{1g} peaks of rutile TiO_2. An infrared thermal imager was utilized to monitor the temperature evolution of TiO_2 coated on the optical fiber during continuous irradiation. For comparative analysis, TiO_2 was also coated on a glass substrate using the same hydrothermal method. In this case, TiO_2 coated on the glass substrate was irradiated by an LED emitting light with a wavelength range of 395–415 nm (output optical power was 12 W). Atomic force microscope equipped with a Kelvin probe was used to investigate the surface photovoltage distributions of the TiO_2 coated on optical fiber and glass substrate.

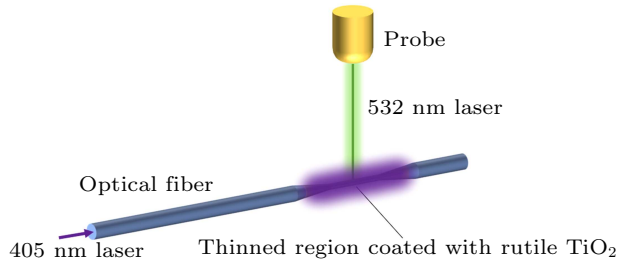


Fig. 1. Schematic illustration of the Raman testing system for rutile TiO_2 coated on an optical fiber.

3. Results and discussion

Figure 2(a) presents the light field distribution of the optical fiber coated with TiO_2, indicating that ultraviolet light is predominantly confined around the TiO_2 layer. Light energy is primarily concentrated within the TiO_2 layer, as evidenced by its higher brightness compared with the surrounding air. Therefore, the interaction between 405 nm light and rutile TiO_2 is enhanced. Figure 2(b) presents the morphology of TiO_2 coated on the optical fiber, showing that TiO_2 exists in the form of nanorods. The lattice fringes with a spacing of 0.324 nm presented in Fig. 2(c) correspond to the (110) planes of rutile TiO_2, indicating that the nanorods grow along the (110) crystal planes.[33] Figure 2(d) presents the UV-visible absorption spectrum of TiO_2, the onset absorption wavelength is 413.1 nm. The calculated bandgap of the TiO_2 is 3.002 eV,

which closely aligns with the reported bandgap of rutile TiO_2 (3.0 eV).[34] Light with a wavelength of 405 nm can induce the photo-excitation of TiO_2, thereby generating carriers.

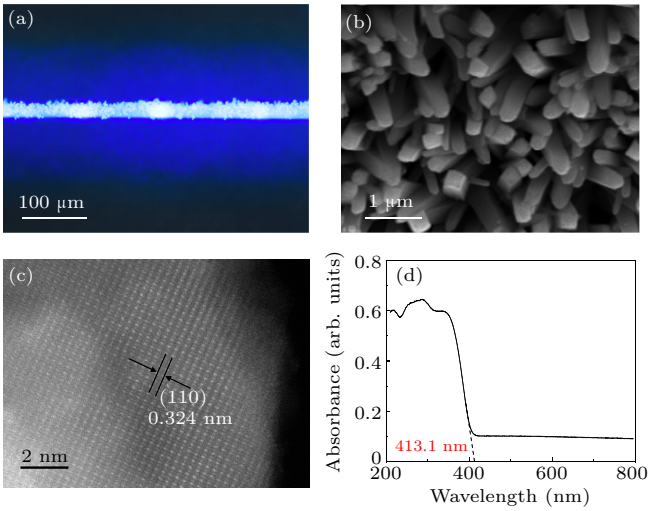


Fig. 2. (a) Light field distribution of the optical fiber coated with TiO_2. (b) Morphology of TiO_2 coated on the optical fiber. (c) TEM image of TiO_2 lattice. (d) UV-visible absorption spectrum of TiO_2.

As shown in Fig. 3(a), the two Raman peaks of rutile TiO_2 coated on the optical fiber before irradiation (irradiation duration is 0 min) are situated at 442.1 cm^{-1} and 606.6 cm^{-1}, corresponding to the E_g peak and A_{1g} peak, respectively. Since the output power (25 mW) of the 405 nm laser source stabilizes after being turned on for 1 min, the Raman spectrum of rutile TiO_2 is initially collected after irradiation for 1 min. The positions of the E_g and A_{1g} peaks exhibit red-shifts under irradiation, and the FWHMs of the two peaks increase (broadening). Specifically, the red-shifts of the E_g and A_{1g} peaks are 7.0 cm^{-1} and 1.9 cm^{-1}, respectively. Additionally, the broadenings of the E_g and A_{1g} peaks are 12.6 cm^{-1} and 11.3 cm^{-1}, respectively. The red-shifts of the Raman peaks indicate a reduction in the frequencies of the corresponding phonons, while the broadenings signify a decrease in the lifetimes of the phonons.[13] Figures 3(b) and 3(c) present the corresponding positions and FWHMs of the Raman peaks, comparing the Raman spectra of rutile TiO_2 acquired at different time points during continuous irradiation. The positions and FWHMs remain relatively stable as irradiation duration increases, suggesting minimal spectral changes. Furthermore, upon turning off the 405 nm laser source, the Raman spectrum returns to its initial state, i.e., the above changes are reversible. This indicates that no new crystalline substances are formed and no phase transformation occurs in rutile TiO_2 during irradiation because these changes are irreversible.

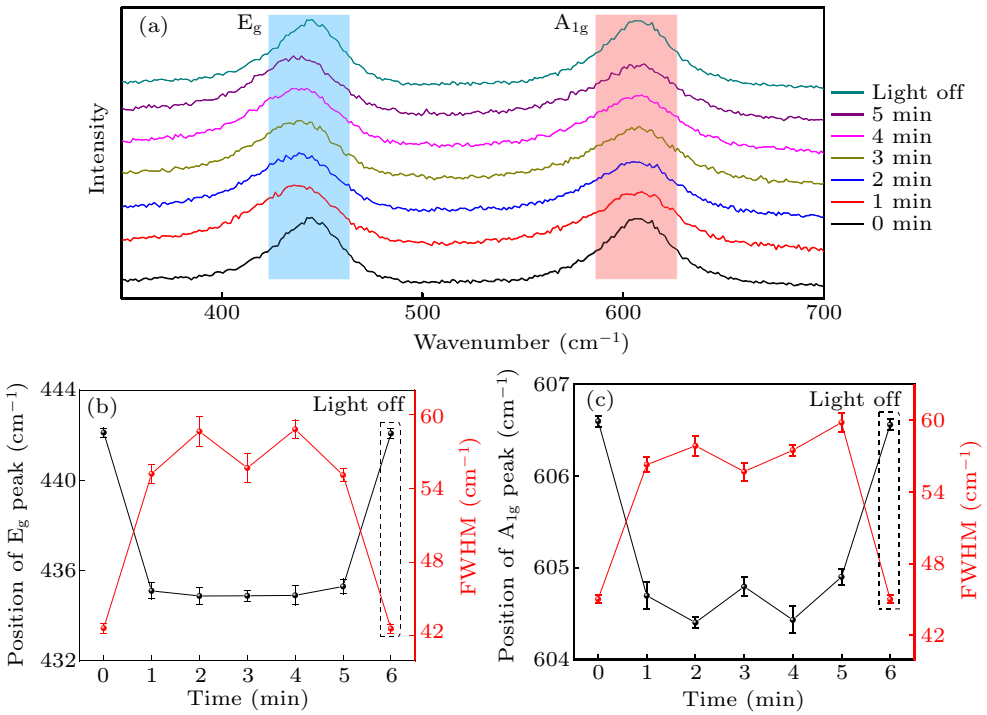


Fig. 3. (a) Raman spectra of rutile TiO_2 coated on the optical fiber at different time points during continuous irradiation (optical power is 25 mW). The position and FWHM changes as a function of irradiation duration: (b) E_g peak and (c) A_{1g} peak.

It has been reported that both overall heating or local heating induced by high-power infrared Raman detection lasers can induce similar changes in the Raman spectra of rutile TiO_2.[24,25] The increase in the macroscopic temperature of rutile TiO_2 results in red-shifts and broadenings of the E_g and A_{1g} peaks. According to the infrared thermal imaging results, the macroscopic temperature of rutile TiO_2 coated on the optical fiber increases from 21.9 °C to 25.9 °C after continuous irradiation for 5 min. Since the wavelength of the light transmitted in the optical fiber is 405 nm, which falls within the ultraviolet spectrum, its thermal effect is significantly weaker compared with infrared light.[35] Furthermore, the thermal ef-

fect of light exhibits a cumulative effect, whereas the Raman spectra of rutile TiO_2 coated on the optical fiber remain relatively stable with increasing irradiation duration. Hence, in this experiment, the thermal effect of irradiation is not the primary factor contributing to the changes in the E_g and A_{1g} peaks.

In previous studies, temperature-induced changes in the E_g and A_{1g} peaks can be attributed to the transfer of energy to the lattice of rutile TiO_2, thereby affecting the phonons.[24,25] As previously discussed, light with a wavelength of 405 nm can excite rutile TiO_2 to generate carriers. Therefore, it is plausible that the alterations in Raman-active vibrational modes result from the interaction between carriers and phonons, wherein the energy of the carriers is transferred to the lattice. Initially, the photo-generated electrons and holes are located at the bottom of the conduction band and the top of the valence band of rutile TiO_2, respectively. Subsequently, the carriers can be trapped by the lattice, with the electrons and holes localized at Ti atoms and O atoms, respectively.[36,37] Both electrons and holes are situated within the bandgap after localization, transferring a portion of their energy to the lattice, which has been confirmed by the DFT calculations in related references.[31,32] Moreover, non-radiative recombination of photo-generated carriers can also transfer energy to the lattice.[38] Hence, the changes of the E_g and A_{1g} peaks in this experiment are primarily attributed to the interaction between carriers and phonons. This analysis also explains why the Raman spectra remain relatively stable during irradiation and revert to their initial state after the cessation of irradiation. Since the Raman spectra are collected in ambient air, recombination emerges as the predominant fate of photo-generated carriers in rutile TiO_2. Under stable optical power, an equilibrium between carrier generation and recombination is maintained, ensuring a consistent carrier population within the lattice. Consequently, a dynamic equilibrium is established in the interaction between carriers and phonons, contributing to the stability of the Raman spectra. Upon cessation of irradiation, the short lifetimes (≤ 1 ns) of the carriers lead to the rapid disappearance of carrier–phonon interaction,[39] resulting in the recovery of the Raman spectrum to its pre-irradiation state.

Figure 4(a) presents the Raman spectra of rutile TiO_2 under varying optical power, while Figs. 4(b) and 4(c) present the parameters of the E_g and A_{1g} peaks, respectively. The redshifts and broadenings of the two Raman peaks become more pronounced with increasing optical power, indicating an enhancement of carrier–phonon interaction. With the increase of optical power (i.e., the number of photons), the number of carriers generated in rutile TiO_2 correspondingly increases. Consequently, the energy transferred to the lattice due to the localization and non-radiative recombination of carriers also increases, thereby enhancing the carrier–phonon interaction.

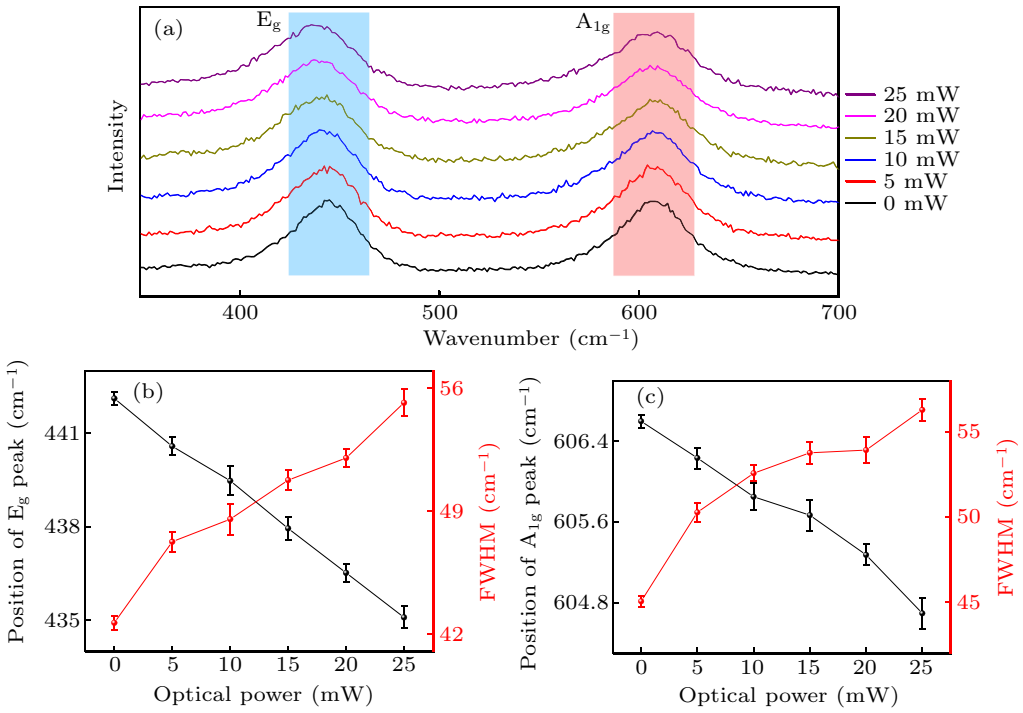


Fig. 4. (a) Raman spectra of rutile TiO_2 coated on the optical fiber under varying optical power. The position and FWHM changes as a function of optical power: (b) E_g peak and (c) A_{1g} peak.

The strength of the chemical bonds associated with a Raman vibrational mode correlates with the wavenumber, i.e., the position of the Raman peak. The Hooke coefficient of a Raman vibrational mode can be calculated using the following equation:[40]

$$k = (2\pi c\bar{\nu})^2 \mu, \tag{1}$$

where k is the Hooke coefficient, c is the velocity of light, $\bar{\nu}$ is the corresponding wavenumber, and μ is the effective mass of Ti–O bond. μ can be calculated through the following equation:[25]

$$\mu = \frac{M_{\mathrm{Ti}} M_{\mathrm{O}}}{M_{\mathrm{Ti}} + M_{\mathrm{O}}}, \tag{2}$$

where M_{Ti} and M_{O} are the atomic masses of Ti and O, respectively. Figures 5(a) and 5(b) present the changes in the Hooke coefficients of the E_g and A_{1g} modes with varying optical power, respectively. When the optical power increases from 0 mW to 25 mW, the Hooke coefficient of the E_g mode decreases from 1.384 N·cm^{-1} to 1.340 N·cm^{-1}, while that of the A_{1g} mode decreases from 2.605 N·cm^{-1} to 2.589 N·cm^{-1}. The decrease in the Hooke coefficients of the Raman-active vibrational modes signifies a weakening of the associated Ti–O bonds, which can result in an elongation of the Ti–O bond lengths. The DFT calculations in relevant references have validated that the lengths of the Ti–O bonds connected to the localized site atoms increase after the localization of carriers.[30,41] The increase in Ti–O bond lengths is associated with tensile stress. The chemical states of the Ti atoms transform from Ti^{4+} to Ti^{3+} after the localization of electrons, while the chemical states of the O atoms transform from O^{2-} to O^{-} after the localization of holes.[30] These changes in the chemical states reduce the Coulomb attraction force between Ti and O atoms, thereby weakening the Ti–O bonds and altering the stress within the lattice.[42–44] The elongation of Ti–O bonds aligns with the weakening of the Ti–O bonds associated with the two Raman-active vibrational modes in this experiment, substantiating that the localization of photo-generated carriers contributes to the red-shifts of the E_g and A_{1g} peaks.

The phonon lifetime of a Raman vibrational mode is inversely proportional to its FWHM. The phonon lifetime can be calculated by using the energy–time uncertainty relation[45]

$$\tau = \frac{\hbar}{\Gamma}, \tag{3}$$

where τ is the phonon lifetime, $\hbar$ is the modified Plank constant (5.3 cm^{-1}·ps), Γ is the FWHM. Figures 6(a) and 6(b) present the variations of the phonon lifetimes for the E_g and A_{1g} modes with optical power. When the optical power increases from 0 mW to 25 mW, the phonon lifetime decreases from 0.124 ps to 0.096 ps for the E_g mode and from 0.118 ps to 0.094 ps for the A_{1g} mode. The reduction in phonon lifetimes can be attributed to the enhancement of phonon–phonon scattering.[13] With the increase of optical power, the quantity of photo-generated carriers increases, subsequently augmenting the number of phonons generated through carrier recombination and strengthening the phonon–phonon scattering. This analysis substantiates that the non-radiative recombination of photo-generated carriers contributes to the broadenings of the E_g and A_{1g} peaks.

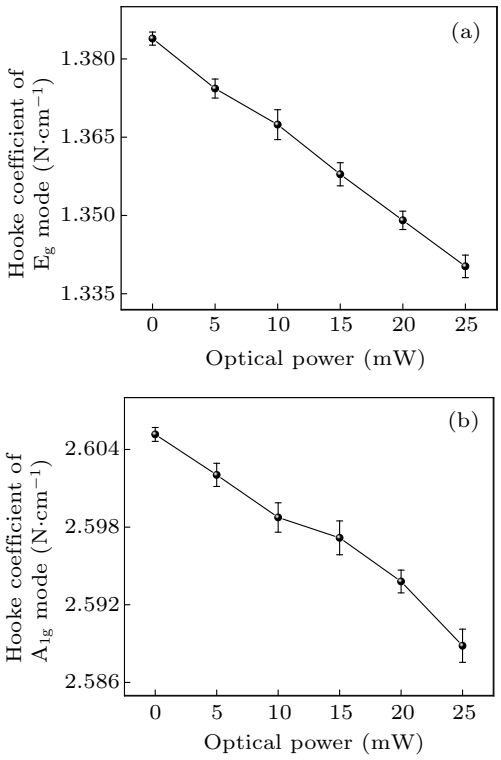


Fig. 5. Variations of calculated Hooke coefficients with optical power: (a) E_g mode and (b) A_{1g} mode.

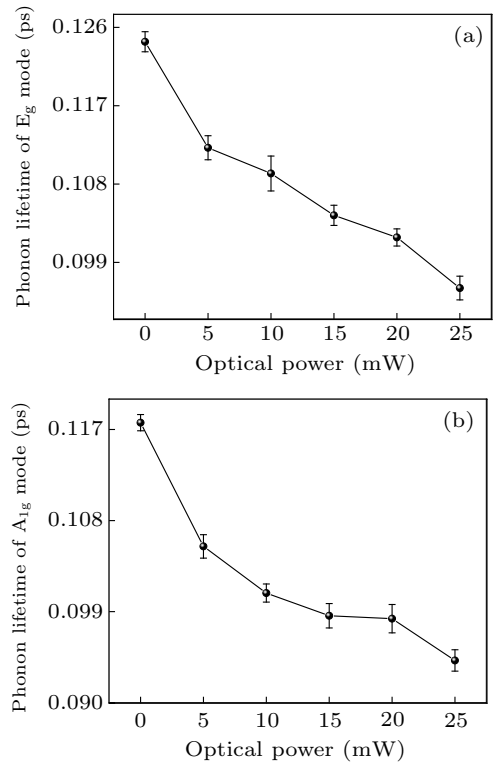


Fig. 6. Variations of calculated phonon lifetimes with optical power: (a) E_g mode and (b) A_{1g} mode.

According to related references,[20,24,25] the changes in the Raman spectra of rutile TiO_2 due to external heating can be attributed to the generation of hot phonons caused by a macroscopic temperature increase, which results in phonon–phonon interaction. In this study, the non-radiative recombination

of carriers generates phonons, which also results in phonon–phonon interaction. It should be noted that the phonons generated by non-radiative recombination can increase the local temperature of the TiO_2 lattice. In contrast to previous studies, this temperature increase is a result of phonon generation rather than its cause. Furthermore, the elevated local lattice temperature can in turn contribute to the changes of Raman spectra. The primary difference between this study and the references lies in the causes of the changes in the Raman spectra. The former is primarily attributed to photo-generated carriers, while the latter is mainly attributed to the increase in macroscopic temperature.

To investigate the impact of light field distribution on carrier–phonon interaction, rutile TiO_2 coated on a glass substrate is irradiated with a LED with a wavelength range of 395–415 nm. Figure 7(a) presents the Raman spectra acquired at different time points during continuous irradiation, while Figs. 7(b) and 7(c) present the corresponding positions and FWHMs of the Raman peaks. After irradiation for 1 min, the red-shifts of the E_g and A_{1g} peaks are 0.6 cm^{-1} and 0.2 cm^{-1}, respectively, accompanied by the broadenings of 2.3 cm^{-1} and 0.9 cm^{-1}, respectively. These changes are notably smaller compared with rutile TiO_2 coated on the optical fiber. Similar to the optical fiber system, as the irradiation duration increases, the positions and FWHMs of the Raman peaks remain relatively stable. The Raman spectrum reverts to its initial state after the cessation of irradiation, i.e., the changes are also reversible.

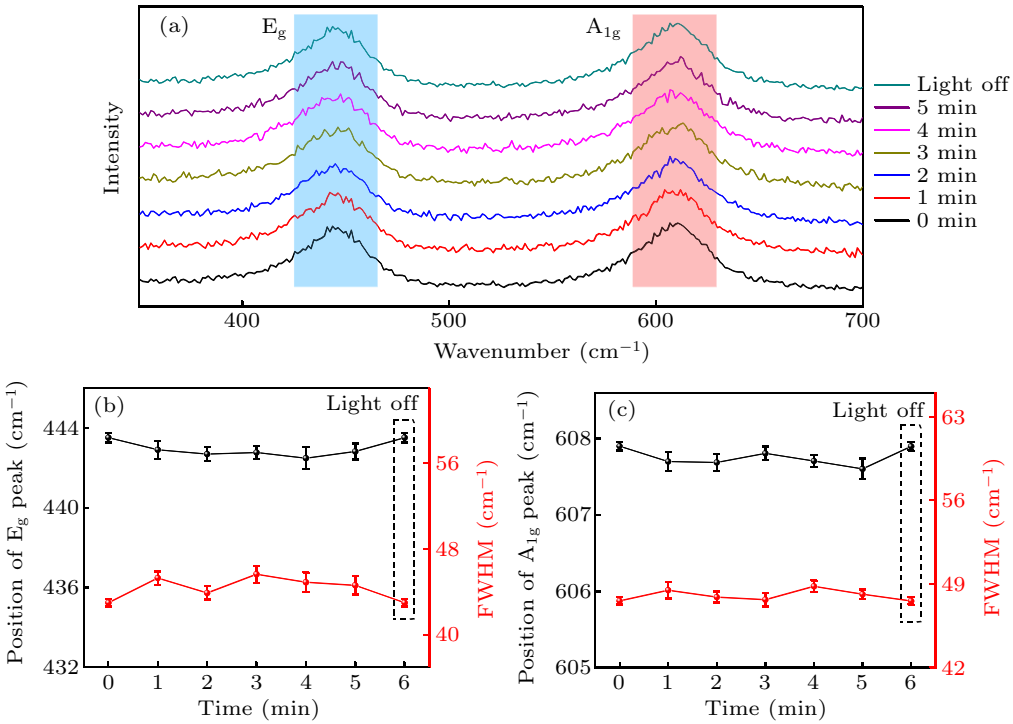


Fig. 7. (a) Raman spectra of rutile TiO_2 coated on a glass substrate at different time points during continuous irradiation (irradiated by LED with a wavelength range of 395–415 nm). The position and FWHM changes as a function of irradiation duration: (b) E_g peak and (c) A_{1g} peak.

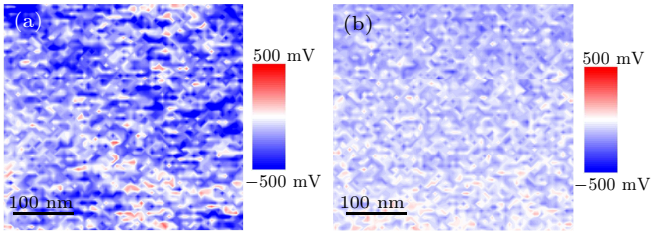


Fig. 8. Surface photovoltage distributions of the rutile TiO_2 coated on (a) thinned optical fiber (optical power is 25 mW) and (b) glass substrate (irradiated by ultraviolet LED).

Figures 8(a) and 8(b) present the surface photovoltage distributions of rutile TiO_2 coated on thinned optical fiber and glass substrate (irradiated by ultraviolet LED), respectively. The average surface photovoltage of the former is −183.2 mV, while that of the latter is −75.8 mV. Since the absolute value of the surface photovoltage reflects the accumulated quantity of surface carriers,[46,47] the quantity of photo-generated carriers in rutile TiO_2 coated on optical fiber is higher than that in rutile TiO_2 coated on glass substrate. This is attributed to the concentrated distribution of light energy in TiO_2 coated on the optical fiber, which improves the generation efficiency and quantity of carriers. This result is consistent with the significantly larger red-shifts and broadenings of the Raman peaks for rutile TiO_2 coated on the optical fiber, indicating that the changes in the Raman spectra are caused by photo-generated carriers. The increase in the quantity of carriers strengthens the carrier–phonon interaction. Coating rutile TiO_2 on thinned optical fiber enhances the changes in Raman spectra, thereby serving as an optimal platform for researching carrier–phonon interaction. Combining a thinned optical fiber with an ultra-

violet laser source enables the miniaturization of the testing setup. Moreover, the use of laser source allows for precise control over the optical power exerted on rutile TiO_2.

4. Conclusions

In this study, the impact of photo-generated carriers on the phonons in rutile TiO_2 is investigated using Raman spectroscopy. Coating rutile TiO_2 on thinned optical fiber can enhance the interaction between ultraviolet light and the material. The E_g and A_{1g} peaks in the Raman spectra of rutile TiO_2 exhibit red-shifts and broadenings under irradiation, indicating a decrease in the frequencies and lifetimes of the corresponding phonons. The minimal macroscopic temperature rise of rutile TiO_2 during continuous irradiation excludes the thermal effect of 405 nm laser as the primary cause of the spectral changes. Based on the DFT calculation results in related references, it is speculated that the localization and non-radiative recombination of photo-generated carriers contribute to the decrease of phonon frequencies and lifetimes. Moreover, rutile TiO_2 coated on the glass substrate exhibits similar changes in Raman spectra under LED irradiation, but the red-shifts and broadenings of the Raman peaks are much smaller than that of the optical fiber system. This discrepancy is attributed to the inefficient concentration of light energy within rutile TiO_2, resulting in lower generation efficiency and quantity of carriers compared with the optical fiber system. Consequently, the carrier–phonon interaction in rutile TiO_2 is weakened. This work provides new insights into the effect of carriers on phonons and proposes a novel approach for researching the behavior of photo-generated carriers in semiconductors.

Acknowledgements

Project supported by the National Natural Science Foundation of China (Grant Nos. 52122008, 51978024, and 52370003) and the Science and Technology and Innovation Commission of Shen Zhen Municipality (Grant No. JCYJ20200109105212568).

References

[1] Zhang X, Tan Q H, Wu J B, Shi W and Tan P H 2016 *Nanoscale* **8** 6435
[2] Hu H T, Flöry T, Stummer V, Pugzlys A, Zeiler M, Xie X H, Zheltikov A and Baltuška A 2024 *Light-Sci. Appl.* **13** 61
[3] Kerdoncuff H, Lassen M and Petersen J C 2019 *Opt. Lett.* **44** 5057
[4] Mondal W R, Evlyukhin E, Howard S A, Paez G J, Paik H, Schlom D G, Piper L F and Lee W C 2021 *Phys. Rev. B* **103** 214107
[5] Kolesnichenko P V, Tollerud J O and Davis J A 2019 *APL Photonics* **4** 056102
[6] Chen D J, Cheng Y L, Zhou N, Chen P, Wang Y P, Li K, Huo S H, Cheng P F, Peng P, Zhang R C, Wang L, Liu H, Liu Y H and Ruan R 2020 *J. Clean. Prod.* **268** 121725
[7] Ni M, Leung M K, Leung D Y and Sumathy K 2007 *Renew. Sust. Energ. Rev.* **11** 401
[8] Junkar I, Kulkarni M, Drašler B, Rugelj N, Mazare N, Flašker A, Drobne D, Humpolíček P, Resnik M, Schmuki P, Mozetič M and Iglič A 2016 *Bioelectrochemistry* **109** 79
[9] Lee J W, Lee T Y, Yoo P J, Grätzel M, Mhaisalkar S and Park N G 2014 *J. Mater. Chem. A* **2** 9251
[10] Xu Z F, Tong C J, Si R T, Teobaldi G and Liu L M 2022 *J. Phys. Chem. Lett.* **13** 857
[11] Xu Y Z, Wang Z, Chen H L and Weng Y X 2024 *J. Phys. Chem. C* **128** 2096
[12] deQuilettes D W, Frohna K, Emin D, Kirchartz T, Bulovic V, Ginger D S and Stranks S D 2019 *Chem. Rev.* **119** 11007
[13] Sahoo S, Ghorai G, Ghosh K, Das B, Sikdar M K and Sahoo P K 2021 *AIP Adv.* **11** 105013
[14] Li Z L, Li Z Q, Zuo C L and Fang X S 2022 *Adv. Mater.* **34** 2109083
[15] Nakata K and Fujishima A 2012 *J. Photoch. Photobio. C* **13** 169
[16] Djokić V R, Marinković A D, Petrović R D, Ersen O, Zafeiratos S, Mitrić M, Ophus C, Radmilović V R and Janaćković D T 2020 *ACS Appl. Mater. Interfaces* **12** 33058
[17] Mitev P D, Hermansson K, Montanari B and Refson K 2010 *Phys. Rev. B* **81** 134303
[18] Abdullah S A, Sahdan M Z, Nayan N, Embong Z, Hak C R and Adriyanto F 2020 *Mater. Lett.* **263** 127143
[19] Parkin W M, Balan A, Liang L, Das P M, Lamparski M, Naylor C H, Rodríguez-Manzo J A, Johnson A T, Meunier V and Drndić M 2016 *ACS Nano* **10** 4134
[20] Rani C, Pathak D K, Tanwar M, Kandpal S, Ghosh T, Maximov M Y and Kumar R 2022 *Mater. Adv.* **3** 1602
[21] Wu Y N, Saidi W A, Ohodnicki P, Chorpening B and Duan Y 2018 *J. Phys. Chem. C* **122** 22642
[22] Swamy V, Muddle B C and Dai Q 2006 *Appl. Phys. Lett.* **89** 163118
[23] Lukačević I, Gupta S K, Jha P K and Kirin D 2012 *Mater. Chem. Phys.* **137** 282
[24] Lan T, Tang X L and Fultz B 2012 *Phys. Rev. B* **85** 094305
[25] Zhang Y L, Harris C X, Wallenmeyer P, Murowchick J and Chen X B 2013 *J. Phys. Chem. C* **117** 24015
[26] Huang Y L, Lee Y T, Yeh V and Cheng C L 2009 *J. Lumin.* **129** 1762
[27] Machon D, Le Bail N, Hermet P, Cornier T, Daniele S and Vignoli S 2019 *J. Phys. Chem. C* **123** 1948
[28] Liu Y J, Y. Zhang, Lei H X, Song J W, H. Chen and Li B J 2012 *Opt. Express* **20** 19404
[29] Chauhan M and Singh V K 2023 *J. Optics* **52** 2285
[30] Di Valentin C and Selloni A 2011 *J. Phys. Chem. Lett.* **2** 2223
[31] Cheng J, VandeVondele V and Sprik M 2014 *J. Phys. Chem. C* **118** 5437
[32] Wang D, Wang H F and Hu P 2015 *Phys. Chem. Chem. Phys.* **17** 1549
[33] Wu S F, Chen C, Wang J M, Xiao J R and Peng T Y 2018 *ACS Appl. Energy Mater.* **1** 1649
[34] Landmann M, Rauls E and Schmidt W G 2012 *J. Phys.-Condens. Matter* **24** 195503
[35] Sarina S, Waclawik E R and Zhu H Y 2013 *Green Chemistry* **15** 1814
[36] Sezen H, Buchholz M, Nefedov A, Natzeck C, Heissler S, Di Valentin C and Wöll C 2014 *Sci. Rep.* **4** 3808
[37] Deskins N A and Dupuis M 2009 *J. Phys. Chem. C* **113** 346
[38] Hassen F, Zaaboub Z, Bouhlel M, Naffouti M, Maaref H and Garni N M 2015 *Thin Solid Films* **594** 168
[39] Dimitropoulos D, Jhaveri R, Claps R, Woo J C and Jalali B 2005 *Appl. Phys. Lett.* **86** 071115
[40] Sunny A, Thirumurugan A and Balasubramanian K 2020 *Phys. Chem. Chem. Phys.* **22** 2001
[41] Zhang L L, Chu W B, Zhao C Y, Zheng Q J, Prezhdo O V and Zhao J 2021 *J. Phys. Chem. Lett.* **12** 2191
[42] Shen S Y, Jiang X X, Zheng Y S, Xue X X, Feng Y X, Zeng J and Chen K Q 2023 *Phys. Chem. Chem. Phys.* **25** 7519
[43] De Lile J R, Bahadoran A, Zhou S and Zhang J J 2022 *Adv. Theor. Simul.* **5** 2100244
[44] You P W, Chen D Q, Liu X B, Zhang C, Selloni A and Meng S 2024 *Nat. Mater.* **23** 1100
[45] Beechem T and Graham S 2008 *J. Appl. Phys.* **103** 093507
[46] Wu M C, Liao H C, Cho Y C, Tóth G, Chen Y F, Su W F and Kordás K 2013 *J. Mater. Chem. A* **1** 5715
[47] Mao J, An X Q, Gu Z N, Zhou J, Liu H J and Qu J H 2020 *Environ. Sci. Technol.* **54** 10323